Journal of Applied Fluid Mechanics, Vol. 18, No. 11, pp. 2730-2741, 2025.
Available online at www.jafmonline.net, ISSN 1735-3572, EISSN 1735-3645.
https://doi.org/10.47176/jafm.18.11.3475

Enhancing Self-priming Efficiency in Vortex Pumps Through Optimization of the Gas-liquid Separation Chamber

Y. Jin[1], L. Feng[1], Re. Lin[2], Ro. Lin[2], J. Cui[1†] and Z. Zhu[1]

[1] *Zhejiang Key Laboratory of Multiflow and Fluid Machinery, Zhejiang Sci-Tech University, Hangzhou, 310018, China*
[2] *LEO Group Pump Co., Ltd., Hangzhou, 310018, China*

†*Corresponding Author Email: jingyucui@zstu.edu.cn*

ABSTRACT

This study investigates the low self-priming efficiency of vortex self-priming pumps through numerical simulation and optimization of the self-priming process, employing the Eulerian-coupled volume of fluid (VOF) method. The analysis focuses on gas-liquid separation characteristics within the pump, with particular attention to the impact of the relative positioning between the separation plate and the resistance plate in the gas-liquid separation chamber (GLSC). To enhance self-priming performance, the study explores how changes in this relative positioning affect the separation efficiency. Furthermore, energy losses within the pump chamber are examined using entropy production theory. The results indicate that the relative positioning of the separation and resistance plates plays a critical role in both gas-liquid separation and self-priming efficiency. Modifying the angle between the two plates significantly alters vortex dynamics and liquid recirculation within the GLSC. Improper positioning of these plates can generate vortices that drastically impair exhaust performance. Optimal gas-liquid separation is achieved when the angle between the plates is set to 25°, which doubles the self-priming efficiency compared to the original design. Entropy production analysis further reveals that the primary sources of energy loss are located in the flow passage, below the resistance plate, and in the area beneath the baffle and the separation plate. These findings provide valuable insights for optimizing the self-priming performance and structural design of vortex self-priming pumps.

Article History

Received March 3, 2025
Revised May 6, 2025
Accepted June 8, 2025
Available online September 3, 2025

Keywords:

Gas-liquid two-phase flow
Vortex pump
Self-priming performance
Entropy production
Self-priming efficiency

1. INTRODUCTION

The vortex self-priming pump is a specialized type of centrifugal pump that utilizes the rotational motion of its impeller to impart kinetic energy to the fluid, thereby driving flow. It is particularly well-suited for applications requiring low flow rates and high heads, such as urban and rural water supply boosting and agricultural irrigation systems. The fundamental structure layout of the pump is illustrated in Fig. 1. The self-priming function of the vortex pump relies on the synergistic interaction between the impeller design, the pump chamber structure, and critical internal components such as the resistance plate and separation plate. During operation, the rotation of the impeller induces vigorous mixing of fluid and entrained air within the flow passage, forming a two-phase gas-liquid mixture. Upon entering the gas-liquid separation chamber (GLSC), the sudden expansion in cross-sectional area leads to a sharp reduction in liquid velocity. Due to its lower density,

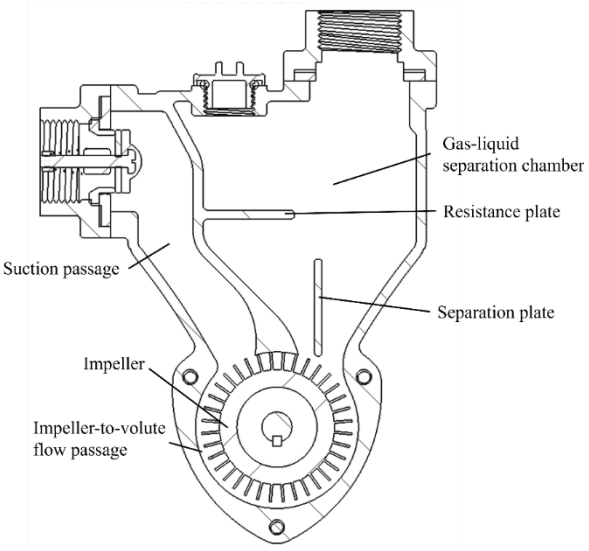

Fig. 1 Basic structure of a conventional vortex self-priming pump

the gas rapidly separates from the mixture and is expelled, while the liquid recirculates into the flow passage to remix with the incoming gas-thus sustaining the continuous self-priming cycle. In this process, the resistance plate plays a crucial role in directing the flow and regulating the local velocities, thereby promoting effective gas-liquid mixing and stable flow conditions. The separation plate facilitates efficient phase separation by guiding the gas for rapid discharge while ensuring the liquid seamlessly returns to the flow passage. This continuous gas-liquid cycle is essential to sustaining the pump's self-priming function. The coordinated design of the resistance and separation plates not only enhances the pump's self-priming performance but also significantly improves its overall operational stability and adaptability under complex operating conditions.

To improve the hydraulic performance and self-priming efficiency of vortex pumps, various optimization techniques have been proposed in recent years. Traditional methods include impeller and volute geometry optimization (Shah et al., 2022), the addition of splitter blades or guide vanes to control internal flow structures (Zhang et al., 2021), and the use of experimental design techniques such as orthogonal arrays to refine key structural parameters (Pei et al., 2016). While these approaches have contributed to performance enhancement, many rely on empirical tuning or trial-and-error, and often lack detailed insights into the underlying flow mechanisms.

While structural optimization techniques have played an important role in enhancing pump performance, a deeper understanding of the internal gas-liquid flow dynamics is essential for guiding such improvements more effectively. In this regard, numerical simulation has emerged as a powerful tool to investigate the complex interactions within gas-liquid two-phase flows in pump systems. These simulation-based approaches not only complement traditional design methods but also provide detailed insights into flow field behavior that are otherwise difficult to capture experimentally.

Currently, the analysis of gas-liquid two-phase flow in pumps mainly relies on numerical simulation methods. Yang et al. (2024a) employed the Multiple-Size Group (MSG) models to simulate gas-liquid two-phase flow within a pump-as-turbine (PAT), investigating the internal flow characteristics, pressure fluctuations, and bubble size distribution. Their results demonstrate that the MSG model effectively captures the complex flow dynamics of gas-liquid two-phase flow systems in PATs and identifies key factors influencing energy recovery. Shi & Rzehak (2018) conducted numerical simulations of bubble dynamics the motion of bubbles within a mixing tank using the Euler-Euler model. They extended existing turbulence and resistance models by incorporating closure relations validated in pipe flow and bubble columns, thereby improving the accuracy of predictions for individual bubble behavior. Their findings confirmed that the improved model accurately describes bubble distribution and flow characteristics within the mixing tank. Cao et al. (2024) also applied the MSG model to examine the impact of the gas phase on internal flow characteristics in an emergency drainage pump. The study revealed that gas mainly accumulates in the impeller region, with large-diameter bubbles fragmenting into smaller ones. Bubbles on the impeller blades tend to migrate toward the middle region near the hub, forming cavities that obstruct flow passages and ultimately reduce pump performance. To further explore the mechanisms behind performance deterioration, Su et al. (2024) used the Eulerian-Eulerian model to study gas-liquid distribution in a centrifugal pump. Through dimensional analysis, they developed a predictive correlation for bubble size based on factors such as inlet gas volume fraction (IGVF), rotational speed, liquid flow rate, and impeller geometry. Their results showed that increasing IGVF leads to gas accumulation at the impeller inlet due to pressure gradient force. In contrast, increasing rotational speed and decreasing liquid flow rate can mitigate cavity formation within the impeller. Caridad et al. (2008) used numerical simulation techniques to analyze the stress experienced by bubbles inside centrifugal pump impellers. Their study found that large bubbles occupy significant space, disrupt normal liquid flow, and reduce overall pump efficiency.

Although computational fluid dynamics (CFD) simulations have been widely applied to various pump types—yielding significant insights into two-phase flow behavior—research specifically focused on vortex pumps remains limited. Li et al. (2010) investigated gas-liquid two-phase flow inside a vortex pump through both simulation and experimental validation. Their study observed that bubbles tended to accumulate on the pressure side of the impeller blades, with bubble concentration increasing alongside the inlet gas volume fraction. More recently, Li (2024) examined the turbulence characteristics of water flow within a vortex pump. Using a specific velocity of 76 modeling one-eighth of the impeller domain, the study aimed to determine flow velocity, head, and efficiency correction coefficients—adjusted based on the impeller's Reynolds number—to reconcile discrepancies between predicted and experimental head values. Compared to conventional vortex pumps, vortex self-priming pumps feature a more intricate chamber structure, which complicates the analysis of gas-liquid separation phenomena. CFD simulations involving turbulent modeling, flow separation, boundary layer effects, and gas-liquid two-phase flow require significant computational resources to ensure both accuracy and efficiency (Laskminarayana, 1996).

In essence, current research on the two-phase flow dynamics within vortex self-priming pumps remains somewhat limited. There exists a notable gap in comprehending the intricate gas-liquid separation patterns within these pumps, particularly concerning the processes of gas exhaustion and liquid return. The efficacy of gas-liquid separation significantly influences the self-priming capability of vortex self-priming pumps. Therefore, a more profound investigation of the mechanisms governing gas-liquid separation, especially focusing on the behavior of the gas-liquid phases during exhaust and liquid return phases, can furnish valuable theoretical insights and practical directions for refining pump designs and enhancing self-priming efficiency. Enhancing the gas-

liquid separation characteristics not only boosts the operational efficiency and reliability of vortex self-priming pumps but also broadens their utility across two-phase flow fields. This expansion offers significant theoretical and engineering advantages.

This research initiative commences by employing numerical simulations to investigate the self-priming process of a specific model of vortex self-priming pump (depicted in Fig. 1). Through fluid dynamics analysis, the study aims to pinpoint the root causes of discrepancies in gas-liquid separation. Subsequently, the research focuses on optimizing the gas-liquid separation efficiency and improving self-priming performance by adjusting the relative positioning of the separation plate and resistance plate within the GLSC. Furthermore, the study delves into the analysis of energy loss characteristics inside the pump chamber utilizing entropy production theory.

2. METHODOLOGY

2.1 Two-Phase Flow Model

The study employs the Eulerian-VOF (volume of fluid) model for conducting multiphase flow simulations (Ghiji et al., 2016; Suh et al., 2018; Yang et al., 2024b). The Eulerian-VOF method tracks the volume fraction of each phase on a fixed spatial mesh, offering high accuracy in capturing dynamic interfaces, which is particularly advantageous for continuous multiphase flows such as air-water systems. In contrast, the Lagrangian approach follows individual fluid particles and is typically more suited to discrete or droplet-based multiphase systems. It becomes less effective for large-scale continuous media with complex interface deformation, where additional treatments are required to handle interface smearing or merging. Considering the highly complex and often diffuse gas-liquid interfaces within the pump chamber, the VOF method provides a more robust and appropriate framework for simulating the two-phase flow behavior in this work.

This research harnesses the hybrid SST k-ω model proposed by Menter et al. (2003) and further discussed by Li et al., (2018) and Guo et al., (2020), for turbulence modeling. Blending the merits of the k-ω and k-ε models, this approach dynamically switches functions in various regions, utilizing the k-ω model proximal to walls for precise calculations and transitioning to the k-ε model in distant areas to enhance computational efficiency. Proficient in handling strongly rotating flows, this model excels in depicting intricate flow patterns and boundary layer properties. Its combined advantages result in excellent performance in simulating multiphase flows, complex fluids, and turbulent boundary layers.

In this context, the gas-liquid two-phase flow continuity equation is articulated as follows, with the gas phase mass conservation equation:

$$\frac{\partial \alpha_g}{\partial t} + \nabla \cdot \left(\alpha_g \rho_g \boldsymbol{u_g}\right) = 0 \tag{1}$$

The liquid phase mass conservation equation is:

$$\frac{\partial (\alpha_l \rho_l)}{\partial t} + \nabla \cdot (\alpha_l \rho_l \boldsymbol{u_l}) = 0 \tag{2}$$

where α_g and α_l denote the volume fractions of the gas and liquid phases, respectively, ρ_g and ρ_l represent the densities of the gas and liquid phases, respectively, $\boldsymbol{u_g}$ and $\boldsymbol{u_l}$ signify the velocities of the gas and liquid phases, respectively.

The gas-liquid two-phase momentum equation is as follows:

For the gas phase:

$$\frac{\partial \left(\alpha_g \rho_g \boldsymbol{u_g}\right)}{\partial t} + \nabla \cdot \left(\alpha_g \rho_g \boldsymbol{u_g} \boldsymbol{u_g}\right) = -\nabla p_g + \nabla \cdot \boldsymbol{\tau_g} + \alpha_g \rho_g \boldsymbol{g} + \boldsymbol{f} \tag{3}$$

For the liquid phase:

$$\frac{\partial (\alpha_l \rho_l \boldsymbol{u_l})}{\partial t} + \nabla \cdot (\alpha_l \rho_l \boldsymbol{u_l} \boldsymbol{u_l}) = -\nabla p_l + \nabla \cdot \boldsymbol{\tau_l} + \alpha_l \rho_l \boldsymbol{g} - \boldsymbol{f} \tag{4}$$

where p_g and p_l denote the pressure in the gas and liquid phases, respectively, $\boldsymbol{\tau_g}$ and $\boldsymbol{\tau_l}$ represent the stress tensor in the gas and liquid phases, respectively, $\boldsymbol{g}$ signifies the acceleration of gravity, and $\boldsymbol{f}$ denotes other external forces.

The gas-liquid interface is tracked using the VOF method with the equation:

$$\frac{\partial \boldsymbol{\alpha_g}}{\partial t} + \nabla \cdot \left(\alpha_g \boldsymbol{u_g}\right) = 0 \tag{5}$$

$$\alpha_l = 1 - \alpha_g \tag{6}$$

The conservation of energy equation, on the other hand, characterizes the total energy variation within a fluid micro-cluster as the sum of external work and heat transfer. When heat transfer is excluded from consideration, the equation governing the turbulent kinetic energy k is expressed as:

$$\frac{\partial k}{\partial t} + U_j \frac{\partial k}{\partial x_j} = P_k - \beta^* k\omega + \frac{\partial}{\partial x_j}\left[(\mu + \sigma_k \mu_t)\frac{\partial k}{\partial x_j}\right] \tag{7}$$

$$P_k = \min\left(\tau_{ij}\frac{\partial U_i}{\partial x_j}, 10\beta^* k\omega\right) \tag{8}$$

where μ denotes the kinetic viscosity, μ_t represents the turbulent kinetic viscosity, σ_k is an adjustable parameter in the turbulent kinetic energy equation for regulating the rate of turbulent kinetic energy transfer, P_k represents the rate of turbulent kinetic energy production, β^* denotes the eddy viscosity correction factor.

The corresponding equation for the specific turbulence dissipation ω, which describes the rate of energy dissipation due to turbulence, is:

Table 1 Main parameters and values of vortex self-priming pumps

Parameter	Numerical value
Blade number	36
Outer diameter of impeller	60 mm
Power	370 W
Inlet tube diameter	25.4 mm
Outlet tube diameter	25.4 mm
Angular velocity	2850 rpm
Maximum flow rate	2 m^3/h
Maximum head	35 m
Rated flow rate	1.2 m^3/h
Rated head	15 m
Maximum suction range	8 m

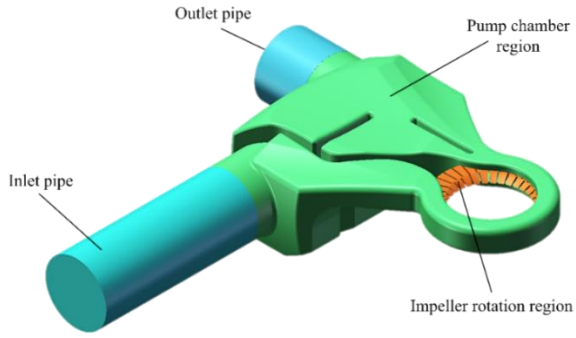

Fig. 2 Fluid computational domain of the original pump model

$$\frac{\partial \omega}{\partial t} + U_j \frac{\partial \omega}{\partial x_j} = \alpha S^2 - \beta \omega^2 + \frac{\partial}{\partial x_j}\left[(\mu + \sigma_\omega \mu_t)\frac{\partial \omega}{\partial x_j}\right] + 2(1 - F_1)\sigma_{\omega 2}\frac{1}{\omega}\frac{\partial k}{\partial x_i}\frac{\partial \omega}{\partial x_i} \quad (9)$$

$$F_1 = \tanh\left\{\{\min\left[\max\left(\frac{\sqrt{k}}{\beta^* \omega y}, \frac{4\sigma_{\omega 2} k}{C\,D_{k\omega} y^2}\right)\right]\}^4\right\} \quad (10)$$

$$C\,D_{k\omega} = \max\left(2\rho\sigma_{\omega 2}\frac{1}{\omega}\frac{\partial k}{\partial x_i}\frac{\partial \omega}{\partial x_i}, 10^{-10}\right) \quad (11)$$

$$\mu_t = \frac{\alpha_1 k}{\max(\alpha_1 \omega, S F_2)} \quad (12)$$

$$F_2 = \tanh\left[[\max\left(\frac{2\sqrt{k}}{\beta^* \omega y}, \frac{500\mu}{y^2 \omega}\right)]^2\right] \quad (13)$$

The term S refers to the total source term in both the turbulent kinetic energy and turbulent dissipation equations. It encompasses the effects of the turbulent kinetic energy production rate P_k on both turbulent kinetic energy and turbulence dissipation rates, as well as other correction terms in the model. The function F_1 is a mixing function, which helps distinguish different flow regimes: a value of 1 corresponds to boundary layer flow, while a value of 0 denotes free shear layer flow. The parameter $\sigma_{\omega 2}$ is a correction coefficient in the turbulent dissipation rate equation, specifically used to adjust the pressure-dependent term of the negative turbulent dissipation rate term.

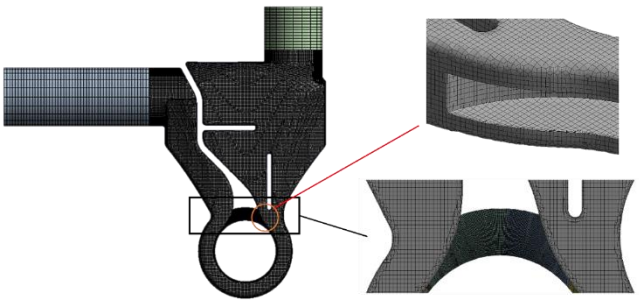

Fig. 3 Generated mesh in our study

2.2 Grid and Time-step Independence Verification

The original configuration of the vortex self-priming pump used in this study (prior to improvements) is shown in Fig. 1, as its key parameters are summarized in Table 1. The computational domain includes the inlet pipe, pump chamber, impeller rotation region, and outlet pipe, as depicted in Fig. 2. Each of these regions was meshed individually. To enhance accuracy, a multi-region meshing approach was adopted for the inlet and outlet pipe regions. Boundary layer meshes were applied along the walls to better resolve near-wall flow behavior. Given the complex geometry of the pump and the need to accurately capture wall effects while maintaining computational efficiency, a relatively fine grid mesh was used in the pump chamber fluid domain. A Cartesian grid method was applied for this part. Additionally, due to the high rotational speed of the impeller and the presence of complex flow patterns within the impeller rotating domain, grid refinement was applied in this region to accurately capture turbulence and flow details. The final generated mesh used for simulations is presented in Fig. 3.

To ensure that the computational results are grid-independent, a grid-independence validation was performed. Eq. (14), defining the mass flow rate, was chosen as the metric for assessing grid independence.

$$m_g = \frac{1}{A}\int \rho_g \boldsymbol{v_g} \cdot d\boldsymbol{A} \quad (14)$$

where $\boldsymbol{A}$ denotes the total area of the selected region, m_g represents the gas mass flow rate, ρ_g denotes the density of the gas, and $\boldsymbol{v_g}$ refers to the velocity vector of the gas.

The results of the grid-independence validation are illustrated in Fig. 4a. Taking into account both computational resources and simulation accuracy, we determined that the solution achieves grid independence at 3.7 million grids. At this grid resolution, the maximum Y^+ value is less than 40 in the impeller area and below 10 in the pump cavity, which aligns with the acceptable thresholds reported in prior studies on pump turbines (Li et al., 2016, 2021; Yang et al., 2023).

In addition to grid-independence validation, we also performed time-step independence validation to determine a suitable time step for transient simulation. Three different

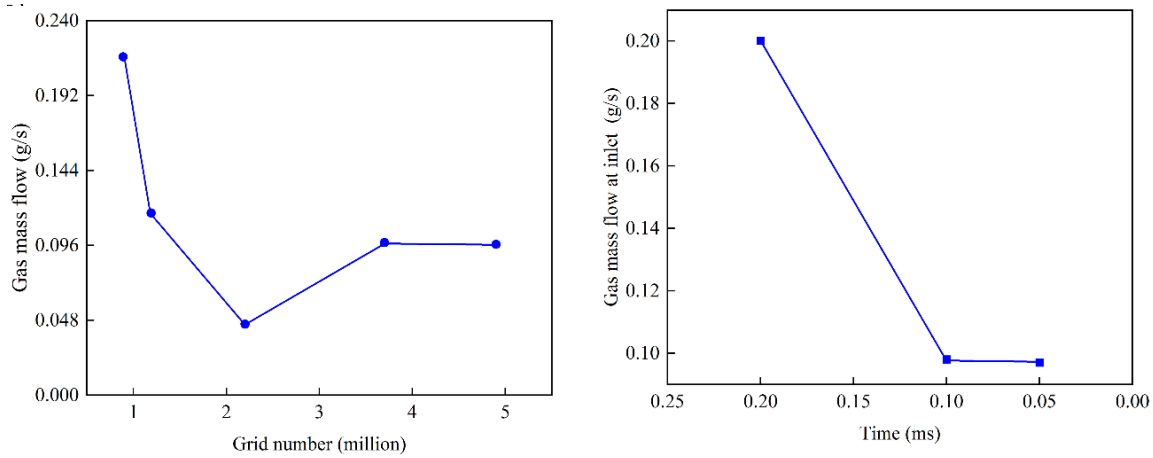

(a) (b)

Fig. 4 (a) Grid-independence verification results, and (b) time-step independence verification results

time steps—5×10^{-5} s, 1×10^{-4} s, and 2×10^{-4} s—were tested. The gas mass flow rate at the inlet was compared at 1.5 s simulation time to evaluate the effect of time step size. As can be seen from Fig. 4b, the gas mass flow rate stabilizes when the time step is 1×10^{-4} s or smaller, indicating that the results are no longer sensitive to time step changes at this resolution. Therefore, considering a balance between numerical accuracy, computational cost, and resource utilization, a time step of 1×10^{-4} s was selected for the final simulations.

2.3 Boundary and Initial Conditions

In the practical self-priming process, the exhaust phase of the vortex self-priming pump extends over a relatively lengthy period (up to several minutes). Given the need for small time steps in two-phase simulations, performing a full simulation of the entire self-priming process would impose an excessive and unnecessary computational load. Considering that, in reality, the pump gradually transitions into a more stable exhaust phase after a certain duration post-startup, which encompasses the majority of the self-priming phase, this study focuses on simulating the process from pump initiation to the point where a stable self-priming state is reached. The target of the simulation is to predict the exhaust velocity after this stable self-priming phase.

To simplify transient simulations and reduce computational complexity, the following assumptions were adopted: (1) the impeller promptly attains its final operating speed upon startup; (2) the inlet pipe, which solely introduces gas at the inlet and is initially filled with gas, aligns with actual self-priming conditions; (3) transient simulations were performed for the initial 1.5 s of the self-priming process, which is sufficient for the pump to reach a relatively stable exhaust phase; (4) the impacts of the baffle and the wall between the impeller and the pump casing were neglected due to the high velocities of the gas-liquid two-phase flow in the flow passage and the low viscosity of gas and liquid water. Moreover, in this study, we focus on the self-priming process of a vortex pump, where the incoming flow is initially gas. The gas-liquid two-phase flow considered here mainly involves the gas-liquid separation behavior

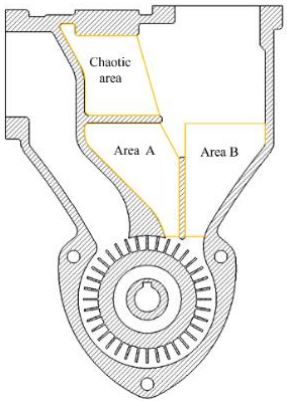

Fig. 5 Division of the internal area of the self- priming pump

during self-priming. The flow regime is dominated by large-scale gas-liquid separation rather than by vaporization-induced cavitation. Even if localized cavitation were to occur, its effect on the self-priming process would be minor compared to the dominant influence of the gas phase. Therefore, cavitation modeling was not included in this work.

In our two-phase simulation, liquid and gas are treated as the primary and secondary phases, respectively. The liquid phase selected in this study was water, and the gas phase was air. Therefore, the conclusions of this study are only applicable to the separation of these two media. Reflecting the operational characteristics of the self-priming phase, the inlet pipe is initially filled with gas, while the pump chamber, impeller, and outlet pipe are filled with liquid. The impeller region is simulated as rotating, whereas all other solid walls are set as stationary no-slip boundaries. Interfaces between the impeller and fluid regions are defined to facilitate data transfer and information exchange. Within the computational domain, both phases start with a velocity of zero, and the initial static pressure at the inlet and outlet is set to atmospheric pressure.

2.4 Optimization Strategy

In Fig. 5, the storage chamber is divided into different regions for analytical convenience. Investigation into the

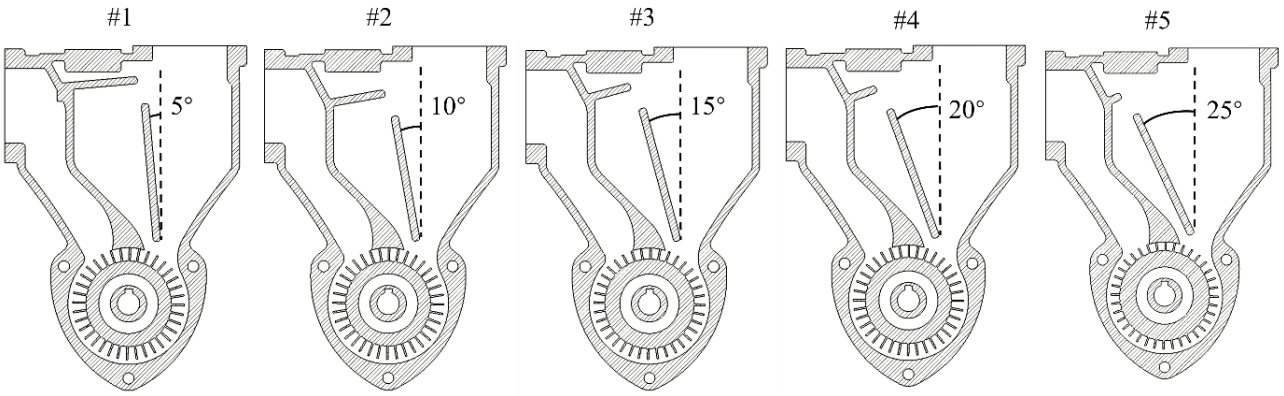

Fig. 6 Five optimization schemes considered in this study, each with a 5°difference in the angle of the separation plate

operational principles of the vortex self-priming pump underscores the pivotal role of gas-liquid separation within the storage chamber in determining the pump's self-priming performance. A successful self-priming process requires effective expulsion of gas to minimize gas retention in the pump, alongside maintaining a smooth liquid flow back into the pump chamber. This dynamic ensures thorough gas-liquid mixing, fostering stability in the circulation process.

In this study, the optimization strategy focuses on improving gas-liquid separation efficiency by adjusting the relative positioning between the separation plate and the resistance plate. Specifically, the angle between these two plates is selected as the sole design variable to isolate its influence on pump performance. Other parameters that may also affect self-priming—such as the size of the opening between the plates and the length of the separation plate—are kept constant to eliminate confounding effects. As shown in Fig. 6, five optimization schemes are considered, each corresponding to a different angular configuration of the separation plate, with a 5° increment between successive schemes.

3. RESULTS AND DISCUSSION

3.1 Characteristics of Gas-Liquid Two-phase Flow in the Pump

In the specific type of vortex self-priming pump under examination, the gas-liquid two-phase flow within the pump chamber is predominantly steered by the centrifugal force and kinetic energy pressure generated by the impeller's rotation. These effects are especially pronounced along the impeller's axial plane. Consequently, we have identified and focused on two distinct cross-sectional planes, illustrated in Fig. 7, to scrutinize the dynamics of the gas-liquid two-phase flow.

Figure 8 illustrates the gas-liquid two-phase flow distribution at t=1.5 s for each of the optimized configurations. In all configurations, the gas and liquid phases undergo initial separation at the impeller outlet due to disparate inertia effects. Notably, the gas phase tends to accumulate in Area A and the region above the resistance plate, known as the chaotic area, while the liquid phase

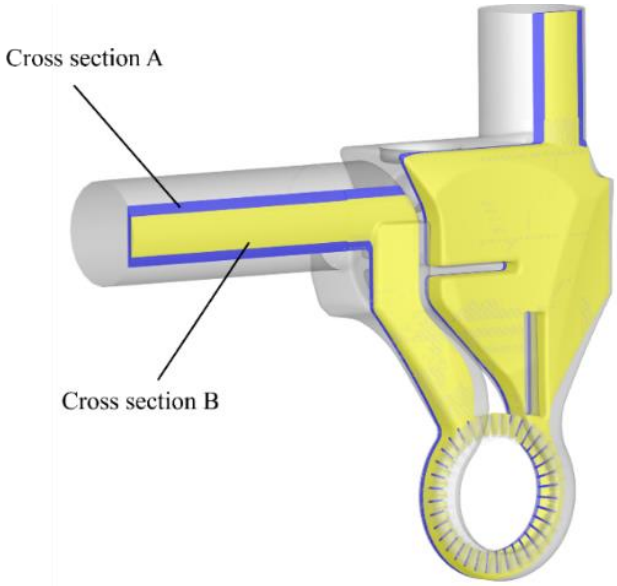

Fig. 7 Two observation planes selected in this study

exhibits higher concentration in Area B. This observation implies that the gas-liquid mixture primarily enters Area A together, where further separation occurs. As the mixture exits Area A through the upper outlet, the gas phase is expelled via the outlet pipe, while the liquid phase recirculates through Area B, returning to the impeller-to-volute passage. The gas-liquid separation efficiency reaches its maximum when the deflection angle of the separation plate is set to 25°, as indicated by the peak gas-phase mass flow rate measured at the outlet of the separation chamber. In this configuration, gas is effectively conveyed by the liquid into Area A with minimal vortex formation (Fig. 9). By the time the mixture reaches Area B, almost all the gas has been separated, leaving only the recirculated liquid. Conversely, with other deflection angles, vortices form in both Area A and Area B (Fig. 9). The gas-liquid mixture passing through these vortex regions experiences less effective separation, leading to gas accumulation. Scheme #2 and #4 additionally produce vortices in the upper region outside Area B, near the outlet pipe, impeding gas-liquid separation significantly and thus affecting the pump's

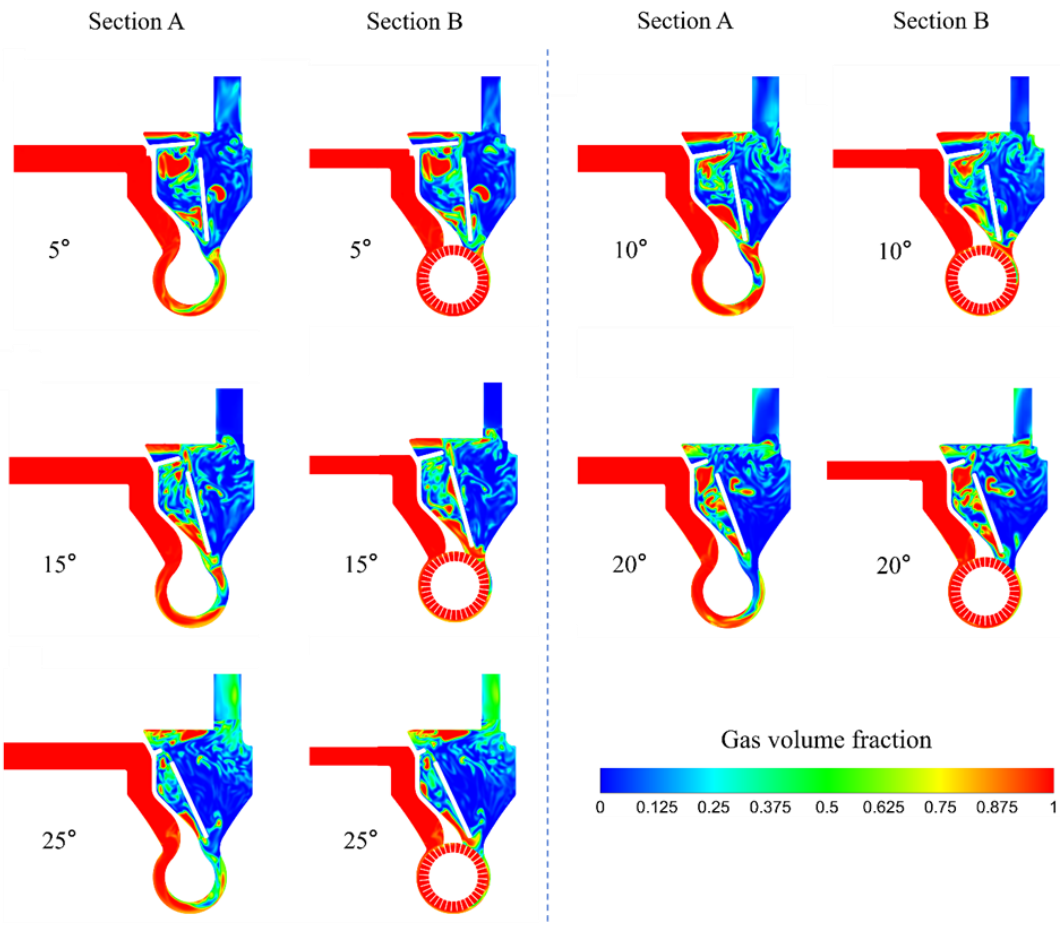

Fig. 8 Gas-liquid two-phase flow distributions in quasi-steady self-priming state

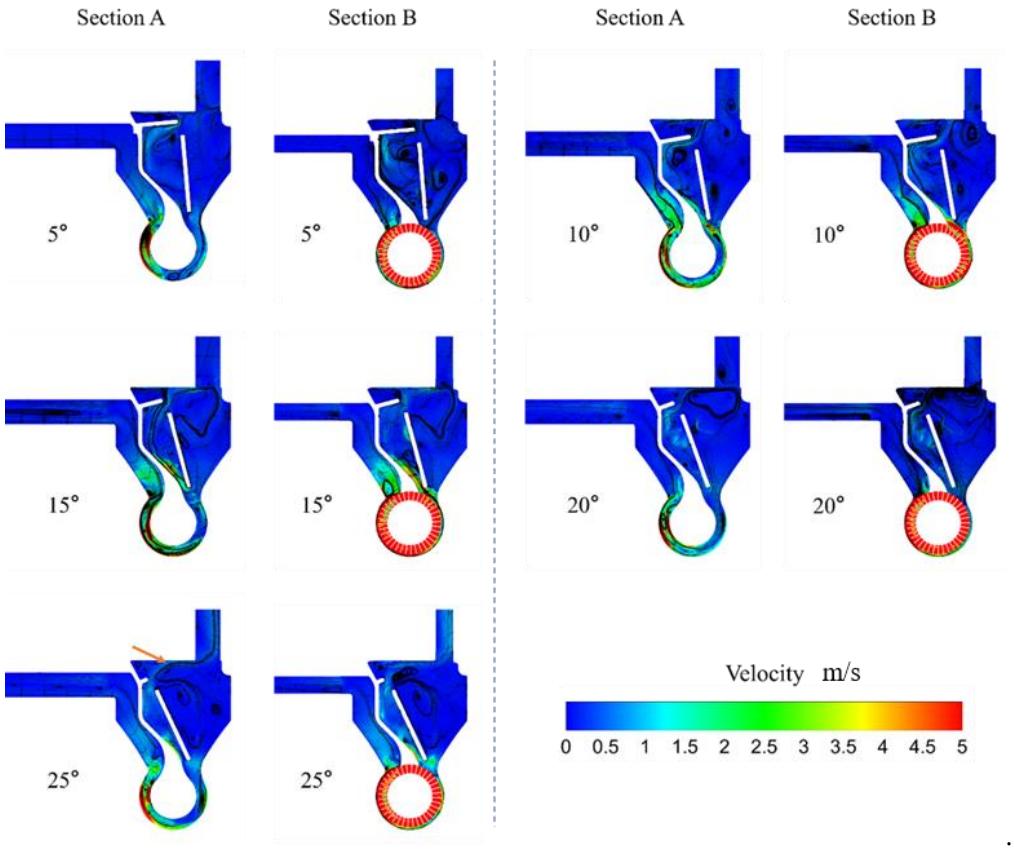

Fig. 9 Simulated velocity contours and streamlines of the liquid phase

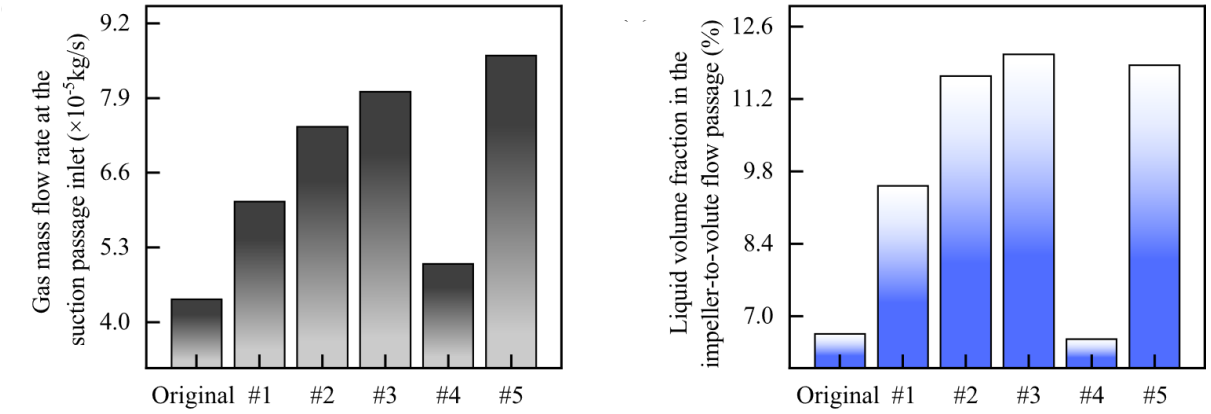

Fig. 10 (a) Time-averaged gas mass flow rate at the suction passage inlet, and (b) time-averaged liquid volume fraction in the impeller-to-volute flow passage

exhaust efficiency negatively. Therefore, the relative positioning of the separation plate and the resistance plate plays a crucial role in determining the self-priming performance of the vortex self-priming pump.

This study concentrates on monitoring the gas mass flow rate at the suction passage inlet over the first 1.5 seconds of the self-priming process. The findings indicate a gradual stabilization of the gas mass flow rate, eventually reaching a quasi-steady state, characterized by fluctuations within a relatively narrow range, with amplitude variations remaining below 5% at the pump inlet. Figure 10a compares the gas mass flow rate at the suction passage inlet between the original and optimized configurations, revealing a non-monotonic relationship between the exhaust gas mass flow rate and the separation plate angle. Initially, adjusting the separation plate angle enhances the gas mass flow rate, which then declines before rising again. The peak exhaust gas mass flow rate occurs at a separation plate angle of 25°, with the gas-liquid separation chamber's enclosed volume representing approximately 15% of the total volume. In contrast, at a separation plate angle of 20°, the exhaust efficiency notably decreases, indicating a less effective separation process. This trend is intrinsically linked to the liquid-recirculation performance of the self-priming pump, with the separation plate angle crucial in determining both gas expulsion and liquid recirculation efficiency. As shown in Fig. 10b, alterations in the separation plate angle cause substantial changes in the pump's liquid-recirculation efficiency. Specifically, the variations in recirculation performance directly correspond to fluctuations in the exhaust gas mass flow rate, as illustrated in Fig. 10a. This highlights that an optimal separation plate angle not only maximizes gas separation but also optimizes the recirculation of the liquid phase, which is crucial for the overall self-priming performance of the pump.

3.2 Internal Energy Loss Analysis

This research delves deeper into the energy loss characteristics in a vortex pump by examining entropy production. By conducting a theoretical analysis of entropy production, this study pinpoints regions of high entropy generation in the flow domain, providing valuable insights for enhancing pump design and optimizing performance. Entropy production is intricately linked to turbulent dissipation and heat transfer dissipation. Turbulent dissipation arises from velocity gradients, while heat transfer dissipation stems from temperature differentials. Given that the vortex self-priming pump typically operates at room temperature with minimal temperature changes, the analysis focuses on isothermal conditions to evaluate energy losses in the pump chamber. Moreover, the Reynolds averaging (RANS) method treats turbulent motion as a blend of time-averaged flow and transient fluctuations. For numerical simulations, the *k-ω* turbulence model is employed. The entropy yield σ caused by turbulent dissipation per unit volume in this method, neglecting heat transfer dissipation, is given by the following expression.

$$\sigma = S_D''' + S_{\bar{D}}''' + S_W'' \tag{16}$$

$$\begin{aligned} S_{\bar{D}}''' = \frac{\mu_m}{T}[(\frac{\partial \bar{u}_2}{\partial x_1} + \frac{\partial \bar{u}_1}{\partial x_2})^2 + (\frac{\partial \bar{u}_3}{\partial x_1} + \frac{\partial \bar{u}_1}{\partial x_3})^2 \\ + (\frac{\partial \bar{u}_2}{\partial x_3} + \frac{\partial \bar{u}_3}{\partial x_2})^2] \\ - \frac{2}{3}\frac{\mu_m}{T}[m(\frac{1}{\rho_1} - \frac{1}{\rho_v})]^2 \\ + 2\frac{\mu_m}{T}[(\frac{\partial \bar{u}_1}{\partial x_1})^2 \\ + (\frac{\partial \bar{u}_2}{\partial x_2})^2 + (\frac{\partial \bar{u}_3}{\partial x_3})^2] \end{aligned} \tag{17}$$

$$S_D''' = \frac{\beta \rho_m \kappa \omega}{T} \tag{18}$$

$$S_W'' = \frac{\tau_W v_W}{T} \tag{19}$$

where S_D''' and $S_{\bar{D}}'''$ denote the pulsation and averaging terms of the entropy production rate under the Reynolds averaging method, respectively, while S_W'' signifies the entropy production change induced by wall shear. T stands for temperature, μ_m denotes the effective dynamic viscosity, $\bar{u}_1 \sim \bar{u}_3$ represent the average velocity components of the fluid in three directions, and $x_1 \sim x_3$ denote the displacement components in three directions. In gas-liquid two-phase flow scenarios, μ_m adheres to the

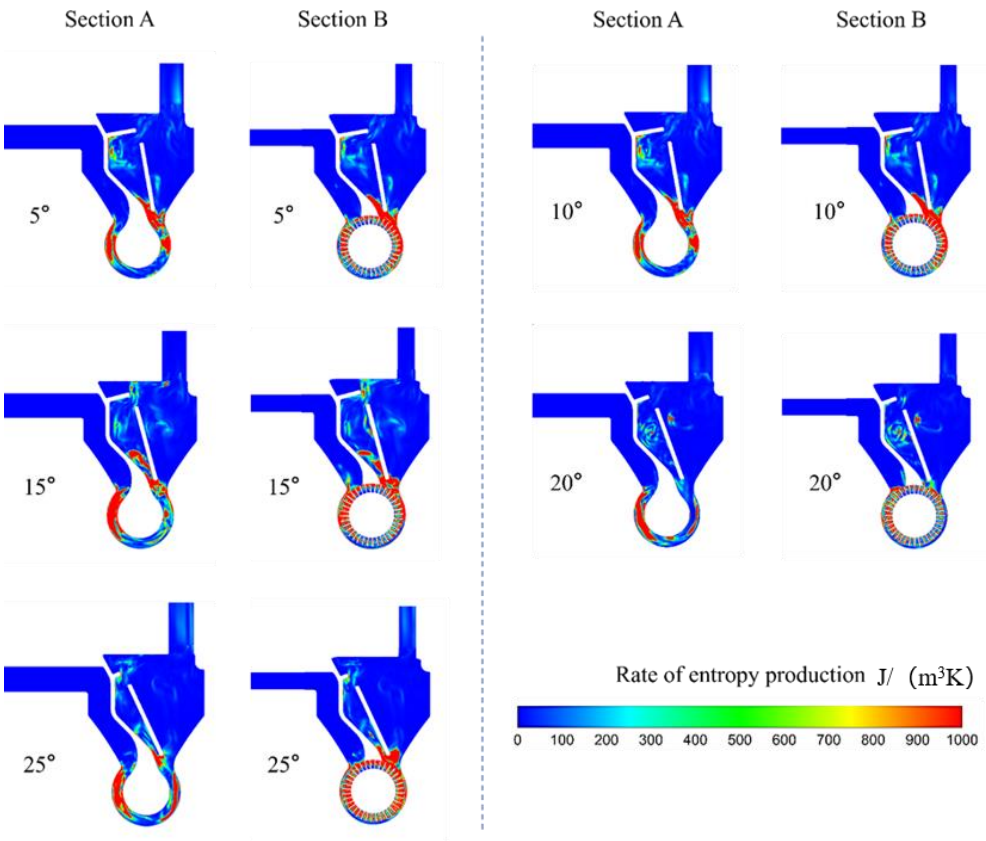

Fig. 11 Distribution of rate of entropy generation in two selected planes

equation $\mu_m = u_l\alpha_l + u_g\alpha_g$, where u_l, α_l, u_g, and α_g stand for the dynamic viscosity and volume fraction of the liquid and gas phases, respectively. The empirical coefficient β, with a value of 0.09 based on the *k*-ω model, relates to turbulent kinetic energy k and turbulent frequency ω. Additionally, τ_W signifies wall shear, and v_W represents the velocity of the first layer grid near the wall.

Figure 11 illustrates the variation and distribution of entropy generation within the pump chamber. Energy losses in fluid systems as per fluid mechanics principles, stem from factors such as frictional resistance, turbulence dissipation, flow disturbances like pipe bends, and changes in cross-sectional areas (e.g., diffusion). These factors contribute synergistically to overall energy dissipation during fluid motion. The energy loss distribution depicted in Fig. 11 highlights three key regions where losses are concentrated: the flow passages, beneath the separation plate, and between the separation plate and the resistance plate. Understanding these areas is crucial for comprehending energy dissipation within the system. In the pump's pressurization chamber, the high impeller rotational speed causes fluid velocity to surpass a critical threshold, transitioning from laminar to turbulent flow. Turbulence introduces vortices and mixing, significantly enhancing energy dissipation in the flow passages. Turbulent eddies and chaotic fluid motions induce high frictional losses, contributing to increased entropy generation. Beneath the separation plate, the sudden fluid volume expansion upon two-phase flow entry into the reservoir leads to a narrowing effect resembling a venturi or throat structure, creating additional local resistance and disrupting smooth flow, resulting in significant energy loss. The complex flow into the reservoir leads to a narrowing effect resembling a venturi or throat structure, creating additional local resistance and disrupting smooth flow, resulting in significant energy loss. The complex flow configuration in this region exacerbates the situation due to intricate velocity and pressure changes from gas-liquid phase interactions.

Between the separation and resistance plates, the flow pattern resembles a bend as the two-phase flow enters the left side of the separation plate with a certain velocity and then exits through the right side, causing irregularities in streamline distribution and non-uniform velocity profiles. These changes lead to local pressure losses from viscous effects and fluid particle collisions, adding to the overall entropy generation.

Upon a comprehensive evaluation, it is evident that the primary areas responsible for energy losses remain consistent across all observed cases. These areas—particularly the flow passages, beneath the separation plate, and between the separation and resistance plates—represent key structural regions where optimization efforts should be focused. Variations in energy loss distribution among five optimization schemes underscore the significant role of the separation and resistance plate positioning and design in shaping the pump's energy loss profile. Adjustments to these components hold promise for reducing energy dissipation and improving overall efficiency of the pump.

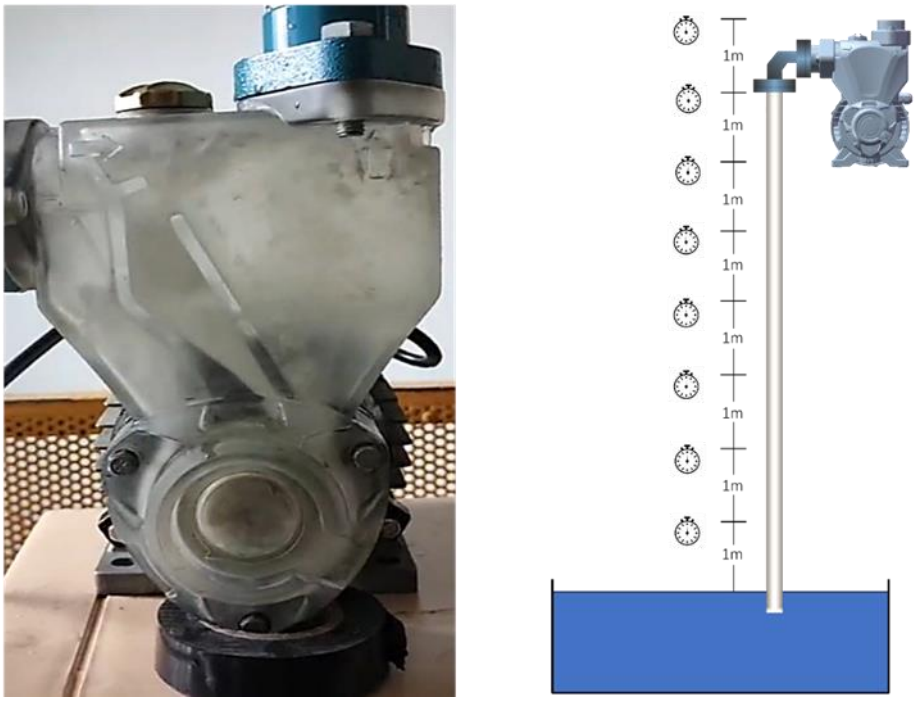

(a) (b)

Fig. 12 Experimental validation of the self-priming effect of the improved model (Scheme #5) (a) Experimental setup (b) Experimental layout for self-priming time test

Table 2 Self-priming experiment test results

Height (m)	Time required for the original model (min)	Time required for Scheme #5 (min)
1	0.42	0.35
2	1.05	0.65
3	1.57	0.93
4	2.15	1.17
5	2.73	1.43
6	3.12	1.68
7	3.58	1.93
8	4.62	2.35
End of self-priming process	4.92	2.47

3.3 Verification of Self-priming Effect and Performance Curve

To validate the accuracy and reliability of the numerical simulation results, tests evaluating self-priming performance were conducted on both the original pump model and the pump model aligned with the optimization strategy displaying superior performance in simulations (referred to as Scheme #5). The experimental setup for this pump is depicted in Fig. 12a, with the experimental layout illustrated in Fig. 12b. During the self-priming phase, a specific volume of liquid in the pump chamber entered the discharge pipe, maintaining a certain height. To achieve this without a check valve at the pump's suction inlet, a vertical pipe greater than 8 meters in height was connected to the pump inlet, considering the pump's critical operational parameters. The liquid surface height was progressively adjusted from 1 m to 8 m, and the time taken for liquid to pass through the outlet was recorded. Under these experimental conditions, the self-priming duration for the original model was approximately 5 min, aligning well with the expected margin of error and meeting standard pump performance evaluation criteria. The pump speed was set at 2850 rpm, and the specific speed was approximately 24.9 r/min. The experimental results indicated that, within the selected time interval, the optimized Scheme #5 demonstrated a notably improved self-priming performance compared to the original model. Specifically, the self-priming efficiency of the optimized pump was approximately twice that of the original model, and the self-priming duration was reduced by around 2 min and 30 s (almost 50% shorter), as outlined in Table 2.

To verify that the improved self-priming performance does not compromise the pump's external performance characteristics, a comprehensive numerical simulation was conducted on both the original and the optimized pump models (i.e., Scheme #5). The results are presented in Fig. 13. As shown in this figure, the head H curves for both models almost completely overlap, indicating that the optimization exerts minimal impact on head performance. Likewise, the efficiency η differences remain negligible at low to moderate flow rates q_v; however, when q_v exceeds 1.8 times the rated flow rate,

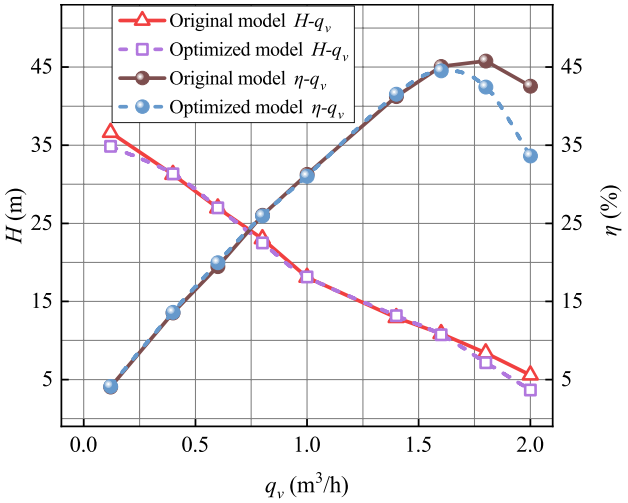

Fig. 13 Simulated pump performance curve

the optimized model exhibits a slight but noticeable decline in efficiency. Nonetheless, the overall performance curve remains essentially unaffected.

In summary, the structural enhancements to the GLSC in Scheme #5 do not significantly impact the pump's overall performance. This clearly demonstrates that the optimized pump model achieves enhanced self-priming performance without sacrificing operational stability. These findings underscore the effectiveness of the proposed optimization strategy in improving self-priming efficiency while maintaining robust performance across a broad range of operating conditions.

4. CONCLUSION

In this study, the Eulerian coupled volume of fluid (VOF) method is employed to numerically simulate the self-priming process in a vortex self-priming pump, with a focus on its gas-liquid separation characteristics. By optimizing the relative positioning of the separation and resistance plates within the gas-liquid separation chamber (GLSC), the gas-liquid separation is optimized to enhance self-priming efficiency. The improved design was subsequently validated through experiments that assessed both self-priming effectiveness and the post-priming performance curve. The primary conclusions of this study are as follows:

(1) The relative positioning of the separation and resistance plates is crucial in directing the two-phase flow inside the pump chamber. Adjustments to the separation plate angle modulate vortex formation: as the angle increases, the vortices within the bounded region decrease while those in other parts of the chamber become more pronounced. This results in an initial improvement, followed by a dip and then a further enhancement in self-priming performance. Specifically, when the angle of the separation plate reaches 25° (with the GLSC enclosing approximately 15% of the total volume), the resulting vortical structure inside the GLSC optimally promotes effective gas–liquid separation and facilitates the return of the liquid to the impeller-to-volute passage. Under these conditions, the self-priming efficiency is significantly improved, with experimental results showing a reduction in self-priming time by approximately 50% compared to the original model.

(2) In the absence of temperature variations, the relative positioning of the separation and resistance plates also influences the distribution of entropy production within the pump chamber. Energy losses caused by fluid motion are primarily concentrated along the impeller flow path, directly below the separation plate, and between its left side and the lower section of the resistance plate. These localized energy losses pinpoint areas of significant flow inefficiency, offering valuable guidance for future design optimizations aimed at minimizing energy dissipation.

In summary, the insights gleaned from this study highlight the critical influence of the separation and resistance plates' geometry on the self-priming efficiency of vortex self-priming pumps. Through targeted design optimizations, it is possible to significantly enhance pump performance without compromising overall operational stability. These advancements pave the way for the development of more efficient and reliable pumps suitable for a broad range of industrial and engineering applications. However, it should also be noted that although experimental validation was performed for the self-priming time, the internal flow field characteristics were not directly measured or visualized in this work. Therefore, flow field observation techniques, such as Particle Image Velocimetry (PIV), are identified as an important direction for future experimental research to further verify the simulation results. In addition, the current optimization focuses only on the relative positioning of the separation and resistance plates. Extending the optimization strategy to other key pump components, such as the impeller and volute, may offer additional performance improvements.

ACKNOWLEDGEMENTS

This work was supported by Zhejiang Provincial Natural Science Foundation of China [Grant No. LD25E060001]; and Science Foundation of Zhejiang Sci-Tech University [Grant No. 22022018-Y]. The authors would also like to sincerely acknowledge LEO Group Pump Co., Ltd. for their generous financial support, which played a crucial role in the successful completion of this research.

CONFLICT OF INTEREST

The authors have no conflicts to disclose.

AUTHORS CONTRIBUTION

Yuzhen Jin: Conceptualization, Writing-Original Draft. **Linhao Feng:** Investigation, Visualization, Validation, Writing-Original Draft. **Renyong Lin:** Resources, Funding acquisition. **Rong Lin:** Resources, Funding acquisition. **Jingyu Cui:** Conceptualization, Supervision, Methodology, Writing-Review & Editing.

Zuchao Zhu: Project administration, Writing-Review & Editing.

REFERENCES

Cao, W., Yang, X., Wang, H., & Leng, X. (2024). Numerical simulation of gas-liquid two-phase flow in emergency rescue drainage pump based on musig model. *Journal of Applied Fluid Mechanics*, *17*(8), 1730-1745. https://doi.org/10.47176/jafm.17.8.2401

Caridad, J., Asuaje, M., Kenyery, F., Tremante, A., & Aguillón, O. (2008). Characterization of a centrifugal pump impeller under two-phase flow conditions. *Journal of Petroleum Science and Engineering*, *63*, 18–22. https://doi.org/10.1016/j.petrol.2008.06.005

Ghiji, M., Goldsworthy, L., Brandner, P. A., Garaniya, V., & Hield, P. (2016). Numerical and experimental investigation of early stage diesel sprays. *Fuel*, *175*, 274. https://doi.org/10.1016/j.fuel.2016.02.040

Guo, G., Zhang, R., & Yu, H. (2020). Evaluation of different turbulence models on simulation of gas-liquid transient flow in a liquid-ring vacuum pump. *Vacuum* *180*. https://doi.org/10.1016/j.vacuum.2020.109586

Laskminarayana, B. (1996). *Dynamics and heat transfer of turbomachinery*. Wiley/ Interscience: New York.

Li, T., Hemida, H., Zhang, J., Rashidi, M., & Flynn, D. (2018). Comparisons of shear stress transport and detached eddy simulations of the flow around trains. *Journal of Fluids Engineering* *140*. https://doi.org/10.1115/1.4040672

Li, W. G. (2024). Effects of interface model on performance of a vortex pump in CFD simulations. https://doi.org/10.1063/5.0196213, *1*, 013901.

Li, W., Ji, L., Li, E., Shi, W., Agarwal, R., & Zhou, L. (2021). Numerical investigation of energy loss mechanism of mixed-flow pump under stall condition. *Renewable Energy*, *167*, 740–760. https://doi.org/10.1016/j.renene.2020.11.146

Li, Y., Zhu, Z. C., He, W. Q., Wang, Y. P., & Cui, B. L. (2010). Numerical simulation and experiment analyses for the gas-liquid two-phase vortex pump. *Journal of Thermal Science*, *19*(1), 47-50. https://doi.org/10.1007/s11630-010-0047-z

Li, Z., Wang, Z., Wei, X., & Qin, D. (2016). Flow similarity in the rotor–stator interaction affected region in prototype and model francis pump-turbines in generating mode. *Journal of Fluids Engineering*, *138* (6), 016201. https://doi.org/10.1115/1.4032298

Menter, F., Kuntz, M., & Langtry, R. (2003). Ten years of industrial experience with the SST turbulence model Turbulence. *Heat and Mass Transfer*, *4*(1), 625-632.

Pei, J., Wang, W. J., Yuan, S. Q., & Yin, T. Y. (2016). Cavitation optimization for a centrifugal pump impeller by using orthogonal design of experiment. *Chinese Journal of Mechanical Engineering*, *29*(5), 992–1002. https://doi.org/10.3901/CJME.2016.1024.125

Shah, M., Baloni, B., & Channiwala, S. (2022). Optimization of centrifugal pump based on impeller-volute interactions. *Advances in Technology Innovation*, *7*(3), 216–227. https://doi.org/10.46604/aiti.2022.8509

Shi, P., & Rzehak, R. (2018). Bubbly flow in stirred tanks: Euler-Euler/RANS modeling. *Chemical Engineering Science* *190*, 419–435. https://doi.org/10.1016/j.ces.2018.06.001

Su, X. B., Xu, Q., Yang, C. Y., Dai, X. Y., & Guo, L. J. (2024). Numerical study of gas pocket distribution and pressurization deterioration mechanism in a centrifugal pump. *Progress in Nuclear Energy*, 177, *17*, Article 105443. https://doi.org/10.1016/j.pnucene.2024.105443

Suh, J. W., Kim, J. W., Choi, Y. S., Kim, J. H., Joo, W. G., & Lee, K. Y. (2018). Development of numerical Eulerian-Eulerian models for simulating multiphase pumps. *Journal of Petroleum Science and Engineering* *162*, 588. https://doi.org/10.1016/j.petrol.2017.10.073

Yang, J., Feng, X., Liu, X., Peng, T., Chen, Z., & Wang, Z. (2023). The suppression of hump instability inside a pump turbine in pump mode using water injection control. *Processes*, *11* (6). 1647. https://doi.org/10.3390/pr11061647

Yang, H., Ying, J. H., Lu, T. Y., Li, L. M., Li, X. J., Wei, Y. K., & Zhu, Z. C. (2024a). Study on characteristics of gas-liquid two-phase flow in pump as turbine using multiple-size group model. *Aip Advances*, *14*(4), 14, Article 045141. https://doi.org/10.1063/5.0206680

Yang, S., Ren, B., Yang, L., Chen, C., Lu, Q., & Wei, Z. (2024b). Investigation of the impact of near-wall mesh size on the transition from microscopic wall boiling mechanism to macroscopic multiphase-CFD models. *Applied Thermal Engineering 244*. https://doi.org/10.1016/j.applthermaleng.2024.122678

Zhang, J., Xiao, Y., Jin, S., Cai, H., & Song, H. (2021). *Effect of guide vane openings and different flow rates on characteristics in pump mode of pump-turbine with splitter blades.* IOP Conference Series: Materials Science and Engineering, 1081(1), 012016. https://doi.org/10.1088/1757-899X/1081/1/012016